The solar noise barrier project 4

Renewable Energy 151 (2020) 1141–1149

Contents lists available at ScienceDirect

Renewable Energy

journal homepage: www.elsevier.com/locate/renene

The solar noise barrier project 4: Modeling of full-scale luminescent solar concentrator noise barrier panels

Ádám Bognár [a], Suryadi Kusnadi [a], Lenneke H. Slooff [b], Chris Tzikas [c], Roel C.G.M. Loonen [a], Minne M. de Jong [c], Jan L.M. Hensen [a], Michael G. Debije [d, *]

[a] Building Physics and Services, Eindhoven University of Technology, 5600 MB, Eindhoven, the Netherlands
[b] ECN, Part of TNO, 1755 ZG, Petten, the Netherlands
[c] TNO - SEAC, High Tech Campus 21, NL-5656, AE, Eindhoven, the Netherlands
[d] Chemical Engineering & Chemistry, Eindhoven University of Technology, 5600 MB, Eindhoven, the Netherlands

ARTICLE INFO

Article history:
Received 24 May 2019
Received in revised form
31 October 2019
Accepted 18 November 2019
Available online 30 November 2019

Keywords:
Luminescent solar concentrator
Noise barrier
Building integrated photovoltaics
Simulation

ABSTRACT

A full-size (1 × 5 m^2) luminescent solar concentrator (LSC) has been constructed and the edge electric outputs from the attached photovoltaic cells monitored for a period of slightly over one year in the solar noise barrier (SONOB) "living lab" outdoor environment. The results of the edge electric output measurements were compared to ray-tracing simulations, revealing imperfections in the system design and production that resulted in the significantly reduced performance of the panel compared to expectations. Results of these calculations suggest edge emission improvements of a factor of 6–9 are possible: at these improved edge outputs, the LSC becomes a viable solar energy generator for the built environment, with significant visual appeal. A grey-box computer model has been developed to predict LSC performance using a realistic device design with reduced internal light scattering and better photovoltaic cell positioning. A second model is used for extrapolation of the LSC solar barrier electric performance with different orientations in different world locations.

1. Introduction

The LSC was introduced as a colorful alternative to traditional silicon-based photovoltaic (PV) panels [1–5]. LSCs are equally capable of handling direct and diffuse light [6], may be produced in a variety of shapes [7–9], and maintain acceptable functionality when operating under high ambient temperatures [10]. The LSC is generally made of a plastic sheet either topped or doped with fluorescent materials, most commonly organic dyes or inorganic quantum dots [4,5]. Sunlight is absorbed by the dye, and the captured energy is subsequently released as a photon with a lower energy. A significant fraction of these emitted photons is trapped in the high refractive index lightguide plate and are funneled towards the edges by total internal reflection. The photons exiting the edges of the plate may then be converted into an electrical current by attached PV cells (see Fig. 1a).

The LSC could find application in the urban setting as a type of building integrated PV (BIPV). The potential for transparency allows for use as windows [11–15], and the increased aesthetic freedom afforded by the colorful panels make possible applications where aesthetics are especially important [9,16–18]. At this time, however, the electrical conversion efficiency of LSCs is only modest [19–21], and must be improved to create real commercial opportunities. The development of large-scale demonstrator modules is necessary for evaluating the performance of LSCs under external climatic conditions.

For this reason, the solar noise barrier project (SONOB) was initiated in which 5 m^2 LSC devices were installed in Den Bosch, the Netherlands. Reports on several aspects of the device performance, including the effects of shading, clouds, and graffiti, have previously been published [22–24]. There have been a number of examples where computer simulation has been used to investigate the performance of LSC devices [8,25–28]. While the results of these simulations corresponded well with measured device outputs, for the most part the work only had access to experimental data for smaller (less than 1 m on a side) devices for comparison. In this work, we employ two LSC computer models to describe and predict performance: one based on ray-tracing, and a grey-box (that is, combining a theory-based model with data from observations).

* Corresponding author.
E-mail address: m.g.debije@tue.nl (M.G. Debije).

https://doi.org/10.1016/j.renene.2019.11.102

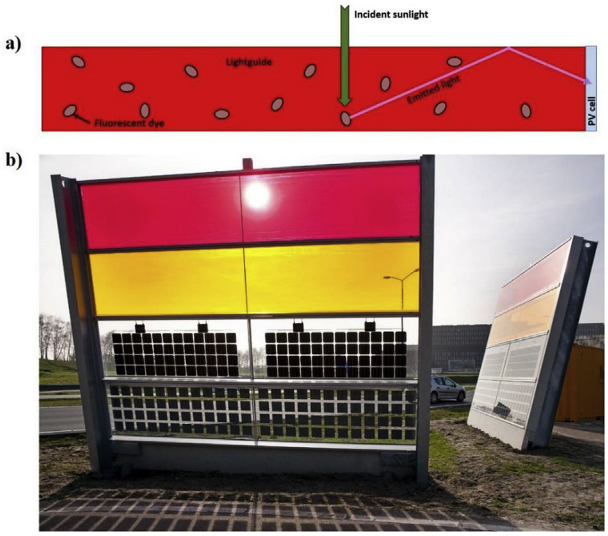

Fig. 1. (a) Schematic showing the basic operation principles of a luminescent solar concentrator. Incident sunlight (green arrow) is absorbed by an embedded dye molecule, which emits the light at a longer wavelength (pink arrow) which travels along the lightguide until exiting the edge of the device and entering an attached photovoltaic cell. (b) Photograph of the test site of the SONOB project in Den Bosch, the Netherlands from behind the East/West facing panel (photo courtesy of Branko de Lang of Heijmans). (For interpretation of the references to color in this figure legend, the reader is referred to the Web version of this article.)

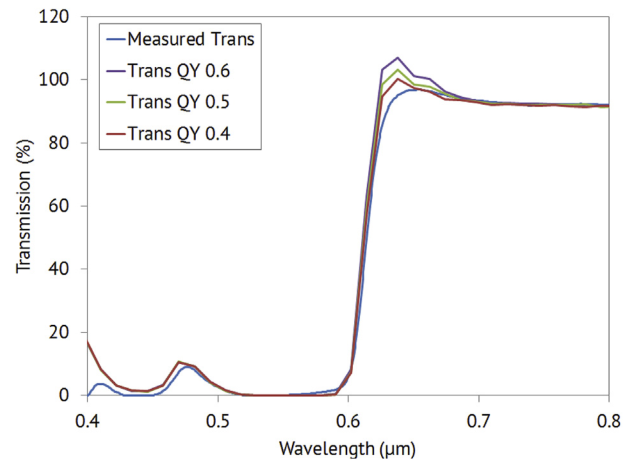

Fig. 2. Comparison of the ray-tracing model with measured transmission data for different assumed effective quantum yields (QY, the number of emitted photons divided by the number of absorbed photons) of the Red305 dye.

The ray-tracing based LSC model is used to examine the physical properties of the plate used in the SONOB project. The ray-tracing calculated edge emissions, which are compared to actual measurements made on the noise barrier panels (see Fig. 1b): we demonstrate that the effective fluorescent quantum yield (QY) of the Lumogen F Red305 (Red305) dye in the full-scale device was significantly lower than anticipated. This finding coupled to our visual inspection of the panels suggest the Red305 was not properly dissolved in the (poly)methylmethacrylate (PMMA), and led to excessive internal losses via scattering of emitted light through the faces. We demonstrate the panels could perform a factor 6–9 times better with better dispersed dye molecules and frame design, which would bring the LSC performance to a level suitable for commercialization.

The grey-box LSC model is used for exploring the performance of a full size, 5 × 1 m^2 SONOB panel containing the commercial Red305 fluorophore from BASF, known to have a QY of at least 98% [29,30]. Using these calculations, we perform a projection of a variety of architectures of the LSC panel under different climatic conditions.

2. Experimental details

To evaluate and analyze the electrical output of the different PV concepts, the Living Lab was equipped with measurement equipment for measuring PV output, solar irradiation, cell temperature and general weather data. For measuring the electrical output of the different PV technologies, we used an EKO MP-160 IV-tracer, in combination with two EKO MI-520 module selectors, each capable of switching 12 IV-channels. The IV-tracer performs a measurement for all 24 channels every two minutes. Simultaneously, the irradiance is measured using 5 EKO MS-802 secondary standard pyranometers, one mounted horizontally, the others mounted in-plane with the barrier, facing in the four natural compass directions. To be able to measure five pyranometer channels, we used an EKO MI-530. Eight T-type thermocouples were used to measure the temperature of a selection of LSC strips and led into an MP-160 through an EKO MI-540 thermocouple selector. A Lufft WS 500 UMB weather station was installed for measuring more general weather data, such as wind speed, precipitation and temperature.

The IV-tracer was controlled by a PC placed in a control container. An internet connection was set up using a 3G/4G internet router. The complete IV data was stored on the local computer. Every 24 h, a summary of the measured data, consisting of irradiance data, Voc, Isc, Vmpp, Impp, cell temperatures and weather data were automatically compiled and sent to the central server.

3. The ray-tracing LSC model

We used a ray-tracing software developed at the Energy Research Centre of the Netherlands (ECN) [23]. In the ray-tracing model, single rays are generated representing light of a specific wavelength travelling in specific directions. A ray incident on an LSC can proceed in two ways, being either reflected or transmitted. During the progress of the ray through the lightguide, the simulation considers reflection and transmission at interfaces, and absorption by the polymer slab and luminescent species. Emission by the luminescent species is dictated by the QY, the emission wavelength (selected from the continuous emission spectrum of the dye used, taking into account that the emission wavelength must be longer than the absorption wavelength), and the direction of the emitted ray selected randomly from the 4π solid angle, which makes it independent of the incident direction (not entirely accurate, but suitable for our purpose [31,32]). Reflection, transmission and internal quantum efficiency (IQE) curves are calculated by monitoring where the rays terminate. Because of the stochastic nature of the ray-tracing process, large numbers of rays (~100,000 per wavelength) must be traced to obtain curves with sufficiently small noise. Previously, it was shown that the ray-tracing program for the LSC was able to accurately describe the experimental results on smaller devices [33].

The ray-tracing model was used to directly explore the performance of the physical device. As the model can currently only be used for direct light, a clear day, May 24th, 2015, was taken for the comparison. The simulation predicted a much higher output power than produced by the actual device. The difference could be explained by either: a) a lower effective QY of the dye than reported in the literature and/or b) the (poly)methyl methacrylate (PMMA) absorbing more light than expected.

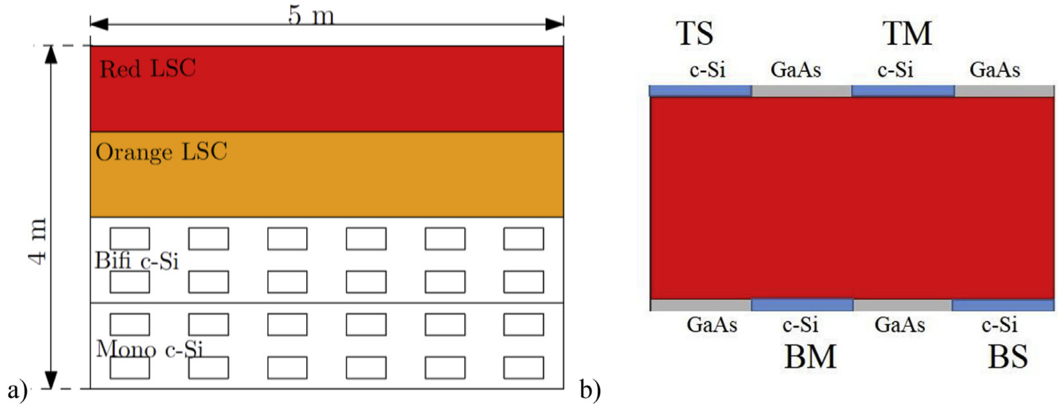

Fig. 3. (a) The global configuration of the solar noise barrier and (b) location of affixed crystalline silicon (c-Si, blue) and gallium arsenide (GaAs, grey) PV cells on the edges of the red LSC. (For interpretation of the references to color in this figure legend, the reader is referred to the Web version of this article.)

After dismantling, transmission measurements through the width of the Red305 LSC lightguide were performed. A comparison of measured and simulated results are shown in Fig. 2 (data for the reflection may be found as Fig. S1 in the Supporting Information). Note the peak around 630 nm: this is the light emitted by the Red305 dye through the rear surface of the lightguide [34]. Normal absorbance of the PMMA lightguide in the emission range of the dye is low [35,36], and there is no indication of extraordinary absorption from the lightguide materials in these panels. From these simulations, it appears clear that the QY of 98% used in the initial calculations for the Red305 panels is not achieved in the actual panels: an effective QY of ~40–50% better matches the measured results.

To confirm the hypothesis of lower effective QY, the edge emission of the SONOB barrier was modeled assuming a standard $0.012 \times 1 \times 5$ m^3 PMMA plate. The plates are oriented to face either East/West (E/W) or North/South (N/S), tilted backwards towards the East or North at 15° with respect to the vertical [22]. A diagram of the panel setups is shown in Fig. 3. The lightguide short edges and the backs of the PV cells along the long edges were covered with 94% reflective white tape (3 M Light Enhancement Film 3635) simulated as a Lambertian scatterer with the same reflection coefficient.

PV cells were connected in series-connected pairs, and the pairs were monitored individually. The Si PV cells are simulated with similar positioning as on the actual device where the small gaps between cells were covered by Lambertian scatterers. The conversion efficiency of photons into electrons was determined by the IQE of typical silicon cells because no IQE spectra of the actual cells were available.

Each day throughout the year, both the elevation (altitude) and azimuth of the sun change, resulting in variation of the light incident on the LSC. In summer, the sun can illuminate the East/West facing LSC from both front and rear, depending on the time of day. The altitude and azimuth of the sun with respect to the plane of the LSC was calculated using the "Sun Position" calculation tool from SunEarthTools [37]. The altitude and azimuth were compared to the orientation of the LSC, taking into account the inclination of the panels towards the North and East. Angles of incidence of light directed towards the backs of the modules (North or West) were converted into angles from the front (South or East) in order to simplify the calculations.

While the current generated in each PV cell-strip was simulated by ray-tracing, the actual device had two PV cell strips connected in series, so the lowest current of the two cell strips was used. The initial calculation assumed an incident power of 1000 W/m^2 on the LSC and a working temperature of 25 °C. The actual incident power was measured by two pyranometers in the plane of the LSC, one on each side. The calculation of performance was done for the 24th of May 2015, which was sunny with mostly direct sunlight. For this reason, only the power from the pyranometer that was positioned at the sun side of the plate was taken, ignoring the contribution from the back. This resulted in some errors at low sun elevations, corresponding to early morning and later afternoon/evening, as the contribution from scattered light during these periods will be relatively large.

The open circuit voltage (V_{oc}) of the PV cells is a function of temperature and current density: for the simulation, the following temperature dependence was used:

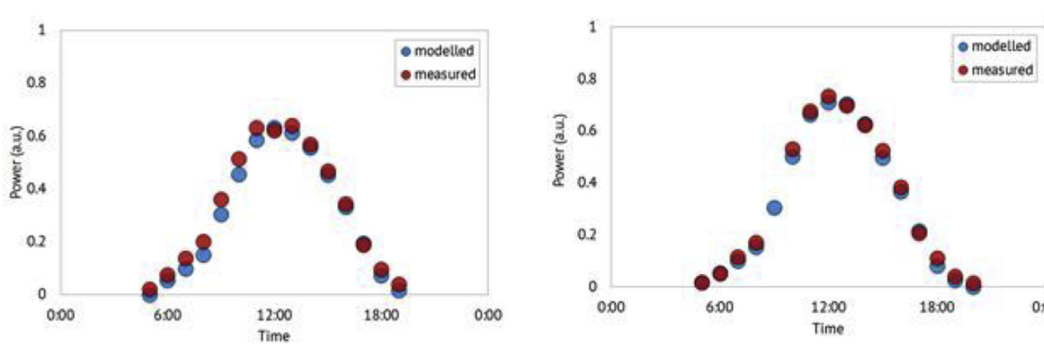

Fig. 4. Calculated (using an effective QY of 50%) and measured power data for a c-Si cell strip on the top (left) and bottom (right) of the North/South oriented Red305 panel for May 24th, 2015. (For interpretation of the references to color in this figure legend, the reader is referred to the Web version of this article.)

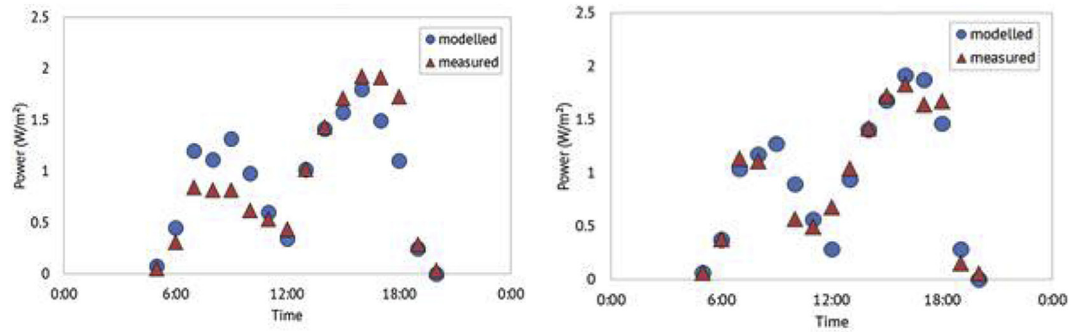

Fig. 5. Calculated (using an effective QY of 50%) and measured power data for c-Si cell strips located at the top (left) and bottom (right) of the East/West oriented Red305 panel for May 24th, 2015. (For interpretation of the references to color in this figure legend, the reader is referred to the Web version of this article.)

$$V_{oc} = \frac{k\,298.13}{q} ln\left(\frac{I_{sc}}{I_0}\right) - 0.0022*(T_{cell} - 298.13) \quad (1)$$

with k being the Boltzmann constant, q the elementary charge, I_{sc} the short circuit current, I_0 the dark saturation current and T_{cell} the cell temperature (in Kelvin). I_0 was taken from a fit to an average I–V curve that was measured on the actual cell strips. The second part in the equation is the decrease in performance as a result of the temperature difference with respect to the cell measurement conditions. A decrease in V_{oc} of 2.2 mV/K was assumed [38]. During the measurement period, the actual PVs reached temperatures exceeding 50 °C. To complete the calculations, the fill factor (*FF*) is determined using a Lambert W function [38,39], and taken as 74% for normal operation conditions.

Fig. 4 shows the comparison between the power output results calculated using an effective QY of 50% and the measured c-Si PV cell strip data from the test site, for the N/S oriented Red305 plates. There are minor differences, but in general the model shows excellent overlap with the measured Red305 data [40]. Similarly, measured and simulated V_{oc} match as well (see Fig. S2).

The data for E/W orientation shows somewhat less overlap, mainly due to self-shading by the side posts of the noise barrier, something not included in the simulation [22]. In Fig. 5a, the cell pair is positioned at the top of the panel, which demonstrates self-shading from the top of the posts in the morning [22]. The bottom position, Fig. 5b, does not suffer from this effect, and consequently the results match better to the actual output. The V_{oc} again matches nicely in Fig. S3.

Poor dye distribution in the SONOB lightguide is likely responsible for the relatively poor performance of the Red305 panels compared to what was anticipated based on the simulations. The lower effective QY in the actual panels could be the result of quenching of the emission by dye agglomerates [41], and additional internal light scattering. Visual inspection of the plates demonstrated that the red panels were indeed quite hazy, although no direct evidence of large dye clusters could be seen under polarized optical microscopy. However, observation of the passage of a red laser beam though the Red305 and Orange240 plates (using wavelengths not absorbed by the dyes) clearly indicate extreme scatter of the beam in the Red305 plate, probably a result of incomplete dye dissolution (see Fig. 6).

The effective Red305 QY of only 40–50% resulted in the significantly reduced power output in the SONOB living lab. The ray-tracing model was used to estimate ideal power outputs of the N/S facing Red305 panel with a normal Red305 QY of 98%: the extrapolated output of the bottom mounted cells could be improved by a factor of 6 (see Fig. 7).

An additional, although more minor, factor limiting the

Fig. 6. Photograph demonstrating scattering of red laser pointed beam by (left) Red305 plate and (right) Orange240 plate from the same noise barrier. (For interpretation of the references to color in this figure legend, the reader is referred to the Web version of this article.)

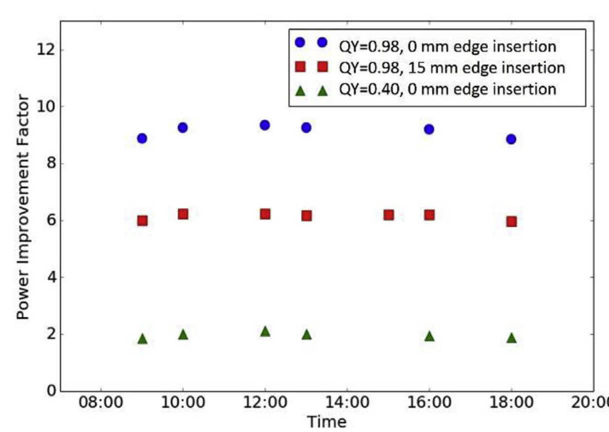

Fig. 7. Calculated improvement factor for c-Si bottom cells attached to the North/South facing Red305 panel when the blocking rim is removed (green triangles), when the effective QY is increased to 98% (red squares) and when both the rim is removed and the QY is set at 98% (blue circles). (For interpretation of the references to color in this figure legend, the reader is referred to the Web version of this article.)

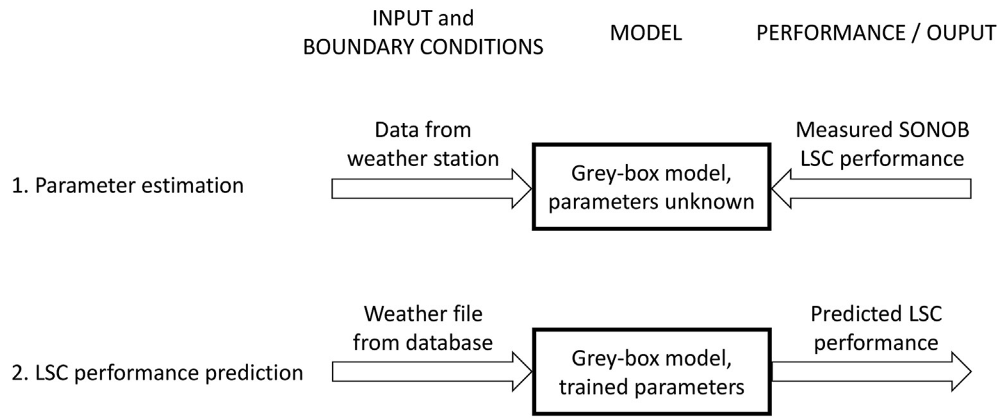

Fig. 8. General setup of the grey-box model used to predict LSC performance.

performance of the outdoor modules was the design of the frame holding the lightguides. The frame secured the plates in place by incorporating a 15–20 mm metal rim around the lightguide edges. This rim prevented illumination of the plate in its covered area closest to the cells, which is usually the most efficient region [42]. By adjusting for both improved dye dissolution in the PMMA and removing of the edge rim of the frame, the LSC output was calculated to improve a total factor of 9 over the measured results, resulting in efficiencies that will allow commercial viability.

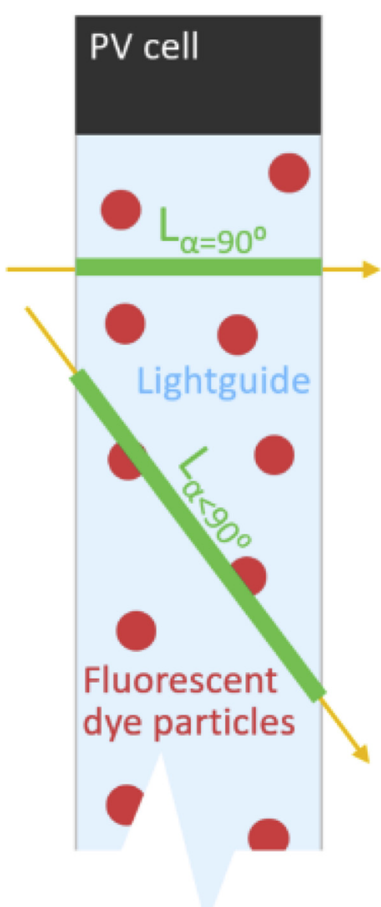

Fig. 9. Photons arriving at a non-perpendicular angle have a larger chance for initial absorption by a dye particle, therefore being utilized, than photons arriving at a perpendicular angle.

4. The grey-box LSC model

We turn now to the development of the model to allow predictions of the performance of device arrays at any specified global location. From what we learned from the ray-tracing work, we look to extrapolate annual performance of idealized LSC modules located in Barcelona, Stockholm and Amsterdam, assuming that production improvements result in less scattering lightguides from the outset.

To determine the annual electricity yield of LSC systems, three transient environmental factors need to be taken into account: solar irradiance incident on both sides of the system, angle of light incidence and the operating temperature of the PV cells. These environmental boundary conditions interact with device-specific characteristics that determine the collection and conversion of irradiance. In this work, these relevant device characteristics are empirically derived from the SONOB set-up, hence the so-called grey-box [43] nature of the model. After the parameters of this grey-box model have been identified, it can then be used for predicting the annual performance of the large-scale LSC system for different orientations and climatic conditions (Fig. 8).

4.1. Description of the grey-box LSC prediction model

The power output of an LSC-PV system (P_{DC}) can be expressed as follows:

$$P_{DC} = G*C_{geo}*\eta_{LSC}*\eta_{PV}*A_{PV}, \quad (2)$$

where G is the total irradiance falling on both sides of the LSC panel. C_{geo} is the ratio between the total surface area and total edge area of glued PV cells, known as the concentration ratio:

$$C_{geo} = \frac{A_{LSC}}{A_{edges}}, \quad (3)$$

where A_{LSC} is the surface area of one side of the LSC panel and A_{edges} is the total surface area, where the PV cells are glued to the edge of the LSC panel. The total conversion efficiency of an LSC system is broken down into two sequential parts: η_{LSC} is the light collection efficiency and η_{PV} is the PV efficiency for converting photons into electrons. A_{PV} is the area of the PV cells at the edge of the LSC panel. The efficiency of PV cells is typically determined under standard test conditions (STC), with fixed irradiance (1000 W/m^2, perpendicular), spectral properties (AM 1.5) and cell temperature (25° C). Real operating conditions are seldom in the STC range, and it is therefore important to consider LSC performance under a wider range of conditions. Moreover, the irradiance is arriving on the two sides of the LSC panel (*f*: front, *b*: back) as separate components of incident light (*dr*: direct, *sd*: sky-diffuse, *gd*: ground-diffuse), which causes η_{LSC} to be dependent on the solar position. Similarly, η_{PV} is dependent on the cell temperature, so equation (3) can be written in the following form:

$$P_{DC} = \sum_{K} \left(G_{s,c} * \varepsilon_{IAM_{s,c}} * \varepsilon_{LP_{s,c}} \right) * C_{geo} * \eta_{LSCopt} * \eta_{PVstc} * \varepsilon_T * A_{PV} \tag{4}$$

for the $K = \{(f,dr); (f,sd); (f,gd); (b,dr); (b,sd); (b,gd)\}$ set of irradiance components. $G_{s,c}$ is a component of irradiance (*dr*, *sd*, or *gd*) for a given side of the LSC plate (*f* or *b*), $\varepsilon_{IAMs,c}$ and $\varepsilon_{LPs,c}$ are the incidence angle [44] and light-path length modifiers for the corresponding side and component. $\varepsilon_{LPs,c}$ is a specific property of the LSC panel expressing that the incoming light passes through a different width of LSC panel when arriving at different angles (see Fig. 9); $\varepsilon_{LPs,c} = 1$ at perpendicular angle of incidence and >1 at non-perpendicular angles. η_{LSCopt} is the optical efficiency of the LSC panel influenced by many factors, including reflection from the front surface, Stokes losses, emission light escaping the surface, and lightguide absorption, among others. η_{PVstc} is the efficiency of the PV cell under STC conditions and ε_T is the temperature correction factor, calculated as:

$$\varepsilon_T = 1 - \frac{\delta}{100}(T_{STC} - T_{cell}), \tag{5}$$

where δ is the temperature coefficient, T_{STC} is the STC temperature, $25^\circ C$ and T_{cell} is the temperature of the PV cell (to be further discussed in Section 3.2). The temperature coefficient depends on the PV technology used. The temperature correction coefficient for mono c-Si PV is around −0.45%/K [45,46].

4.2. Model parameter estimations

The empirical part of the grey-box LSC prediction model is established from experimental output data of the SONOB project in the living lab environment from 30 June 2015 until 30 May 2016. In this study, only the outputs of c-Si PV on the edge of the LSC with N/S orientation are used, along with corresponding data from the pyranometers, thermocouples, and on-site weather station. All the devices recorded output data every 2 min, each day from 03:00 until 22.00. The four c-Si PV on the edges of the red LSC are abbreviated according to their position, as shown in Fig. 2b.

Table 1
The optical efficiency of LSC under direct radiation at TM position for different irradiance and AoI.

Irradiance (kW)	AoI									Median of total
	0-10	10 - 20	20-30	30-40	40-50	50-60	60-70	70-80	80-90	
0.0-0.1							1.79	1.74	1.41	1.62
0.1-0.2							1.06	1.19	1.23	1.21
0.2-0.3					1.42	1.59	1.50	1.88	1.32	1.50
0.3-0.4			3.04	2.84	1.72	1.50	2.22	2.05	1.32	1.98
0.4-0.5		3.06	3.21	1.93	2.71	2.26	2.51	2.07		2.33
0.5-0.6		2.71	1.93	1.92	2.15	2.61	2.46	1.98		2.44
0.6-0.7	1.93	2.14	1.91	1.92	2.74	2.67	2.39			2.57
0.7-0.8	2.03	1.96	2.03	2.54	2.72	2.61	2.23			2.61
0.8-0.9	1.88	2.04	2.43	2.76	2.70	2.53				2.67
0.9-1.0	2.12	2.52	2.70	2.73	2.70	2.50				2.67
1.0-1.1	2.10	2.54	2.63	2.58	2.64					2.60
1.1-1.2		2.41	2.47	2.54	2.47					2.49
1.2-1.3				2.06						2.06
Median of total	2.05	2.47	2.63	2.69	2.70	2.60	2.43	2.00	1.24	2.46

Table 2
The optical efficiency of LSC under direct radiation after correction at TM position for different irradiance and AoI.

Irradiance (kW)	AoI									Median of total	Error
	0-10	10 - 20	20-30	30-40	40-50	50-60	60-70	70-80	80-90		
0.0-0.1							1.79	1.74	1.41	1.62	21%
0.1-0.2							1.06	1.19	2.03	1.83	10%
0.2-0.3					1.08	1.25	1.27	1.92	2.18	2.02	1%
0.3-0.4			2.36	2.17	1.30	1.18	1.87	2.10	2.18	2.03	1%
0.4-0.5		2.53	2.50	1.47	2.06	1.78	2.11	2.12		2.09	2%
0.5-0.6		2.24	1.50	1.46	1.63	2.05	2.07	2.03		2.02	1%
0.6-0.7	1.93	1.77	1.49	1.46	2.08	2.10	2.01			2.03	1%
0.7-0.8	2.03	1.63	1.58	1.93	2.07	2.05	1.88			2.02	1%
0.8-0.9	1.88	1.69	1.89	2.10	2.05	1.99				2.04	0%
0.9-1.0	2.12	2.09	2.10	2.08	2.05	1.96				2.07	1%
1.0-1.1	2.10	2.10	2.05	1.97	2.00					2.03	1%
1.1-1.2		2.00	1.92	1.94	1.87					1.93	6%
1.2-1.3				1.57						1.57	23%
Median of total	2.05	2.05	2.05	2.05	2.05	2.05	2.05	2.05	2.05	2.05	

The aim is to generalize the results of the SONOB measurements in order to be able to predict the performance of an LSC-PV system with the same technical parameters as the device in the SONOB project but under different climates and different tilts and orientations. In equation (4), $G_{s,c}$ is known from on-site measurements. C_{geo} is known from the geometry of the device: the A_{LSC} of the SONOB LSC is equal to $5m \times 1m = 10m^2$, and A_{edges} has an area of $2 \times 5m \times 0.012m = 0.12m^2$. The 8 PVs are installed with the same size of $0.12m^2 \div 8 = 0.015m^2$ on the top and bottom edge of the LSC. Assuming all the PVs collect the same amount of irradiance (which is not quite true, but serves the general nature of this work) [47], the A_{LSC} for each PV is equal to $5m \times 1m \div 8 = 0.625m^2$. Thus, the C_{geo} for each PV in the edge of the LSC is $0.625m^2 \div 0.015m^2 = 41.66$. The η_{PVstc} is set at 0.18, the approximate efficiency for the PV cells supplied for this project, and P_{DC} is measured on site. $\varepsilon_{IAM_{s,c}}$, $\varepsilon_{LP_{s,c}}$ and η_{LSCopt} are unknown parameters. The former two are the function of AOI and the latter is a constant, depending on the material properties of the LSC, but not affected by the AOI or level of irradiance.

As a first step, let's assume, that $\varepsilon_{IAM_{s,c}} * \varepsilon_{LP_{s,c}} = 1$. Using this assumption, the only unknown parameter left in equation (4) is η_{LSCopt}: therefore, we can calculate it's value. Table 1 shows the calculated η_{LSCopt} values under clear sky conditions.

We know that at AOI ≈ 0, $\varepsilon_{IAM_{s,c}} * \varepsilon_{LP_{s,c}} = 1$. Therefore, at times

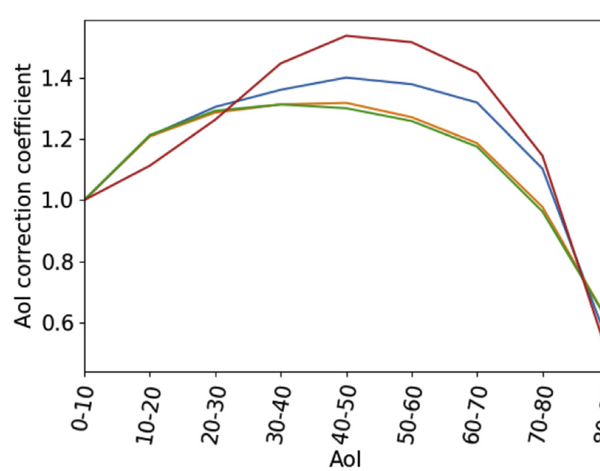

Fig. 10. $\varepsilon_{IAM_{s,c}} * \varepsilon_{LP_{s,c}}$ as a function of angle of incidence for TS(green), TM (orange), BS(red), BM(blue). (For interpretation of the references to color in this figure legend, the reader is referred to the Web version of this article.)

Table 3
Estimated yearly electric energy generation in kWh/year for different tilts and orientations in Amsterdam for a) the LSC system (QY = 98%, η_{PV} = 18%), b) PV (η = 18%) and c) Bifacial PV (η = 18%).

a) **LSC, QY=98%, η_{PV}=18%** — Panel orientation (°)

Panel tilt (°)	~360	~350	~340	~330	~320	~310	~300	~290	~280	~270	~260	~250	~240	~230	~220	~210	~200	~190	~180
	0	10	20	30	40	50	60	70	80	90	100	110	120	130	140	150	160	170	180
0	168	168	168	168	168	168	168	168	168	168	168	168	168	168	168	168	168	168	168
10	156	156	157	158	159	160	162	164	166	168	170	172	174	176	177	178	179	180	180
20	143	144	144	146	148	151	154	158	161	165	169	173	177	180	183	185	187	188	189
30	133	133	134	136	139	143	148	153	158	163	168	173	178	182	186	189	191	193	194
40	126	126	128	130	134	139	144	150	156	161	167	172	177	182	186	190	193	195	196
50	124	124	126	129	134	139	145	150	156	161	166	171	176	181	186	190	193	196	197
60	128	129	131	135	140	144	149	153	157	162	166	171	175	180	184	188	191	193	194
70	139	140	143	146	149	151	154	157	160	163	166	169	173	176	179	182	185	187	188
80	154	155	156	157	159	160	161	162	163	164	166	168	169	171	173	175	177	178	179
90	167	168	169	169	168	168	167	166	165	165	165	165	165	165	166	166	166	167	168

b) **PV, η=18%** — Panel orientation (°)

Panel tilt (°)	~360	~350	~340	~330	~320	~310	~300	~290	~280	~270	~260	~250	~240	~230	~220	~210	~200	~190	~180
	0	10	20	30	40	50	60	70	80	90	100	110	120	130	140	150	160	170	180
0	841	841	841	841	841	841	841	841	841	841	841	841	841	841	841	841	841	841	841
10	762	762	765	770	777	786	796	808	821	834	847	861	873	885	895	903	910	914	916
20	675	675	680	689	702	719	740	762	787	812	838	863	887	909	928	944	957	965	969
30	588	589	596	608	627	651	680	712	747	782	817	852	885	915	942	965	982	994	999
40	506	507	516	533	557	588	624	663	704	746	788	829	868	905	937	965	986	1000	1007
50	434	436	449	471	501	536	574	616	661	706	752	796	839	878	914	945	969	985	993
60	383	387	404	428	458	491	529	571	615	661	707	753	796	838	874	906	931	948	956
70	358	362	376	396	422	452	487	526	568	612	657	700	743	782	819	849	873	890	899
80	338	342	353	369	390	416	447	481	519	560	600	641	680	717	749	777	798	814	822
90	320	323	331	344	361	382	407	437	470	504	541	575	610	641	669	692	709	721	728

c) **Bifacial PV, η=18%** — Panel orientation (°)

Panel tilt (°)	~360	~350	~340	~330	~320	~310	~300	~290	~280	~270	~260	~250	~240	~230	~220	~210	~200	~190	~180
	0	10	20	30	40	50	60	70	80	90	100	110	120	130	140	150	160	170	180
0	1051	1051	1051	1051	1051	1051	1051	1051	1051	1051	1051	1051	1051	1051	1051	1051	1051	1051	1051
10	974	974	977	982	989	998	1008	1020	1033	1046	1060	1073	1085	1097	1107	1115	1122	1126	1128
20	896	896	901	910	923	940	960	983	1007	1032	1057	1082	1105	1127	1146	1162	1175	1183	1187
30	833	833	839	851	868	892	920	952	985	1018	1052	1085	1116	1145	1171	1193	1210	1221	1227
40	792	792	799	813	836	865	900	936	974	1011	1048	1084	1119	1152	1181	1206	1226	1240	1247
50	774	776	787	807	836	869	904	939	976	1011	1046	1081	1115	1147	1177	1203	1224	1239	1246
60	796	801	818	844	871	899	927	957	986	1016	1046	1075	1103	1133	1159	1184	1203	1217	1225
70	869	875	890	909	927	944	963	982	1002	1023	1044	1065	1087	1107	1129	1148	1165	1177	1184
80	960	966	975	983	990	996	1003	1010	1020	1029	1039	1051	1062	1075	1087	1100	1110	1118	1124
90	1048	1052	1055	1055	1052	1048	1042	1039	1036	1033	1033	1032	1033	1034	1037	1039	1042	1044	1048

when AOI ≈0, as in the first column of Table 1, the value of the calculated η_{LSCopt} should be correct. Here we have to note that the irradiance incident on the LSC surface has 6 components, as described earlier; therefore the AOI shown in Table 1 only represents the angle of incidence of the direct component. The sky- and ground-diffuse components also have their own effective angle of incidence on both sides of the LSC panel, introducing some inaccuracies to these calculations.

The next step is to introduce a $\varepsilon_{IAM_{s,c}} * \varepsilon_{LP_{s,c}}$ with a non-unity value. The value of $\varepsilon_{IAM_{s,c}} * \varepsilon_{LP_{s,c}}$ is calculated for each AOI-range shown in Table 2, as $\varepsilon_{IAM_{s,c}} * \varepsilon_{LP_{s,c}} = \eta_{LSCopt}(AOI) / \eta_{LSCopt}(AOI \approx 0)$. The resulting $\varepsilon_{IAM_{s,c}} * \varepsilon_{LP_{s,c}}$ is shown in Fig. 10. Table 2 shows the calculated η_{LSCopt} using equation (4), with the values for $\varepsilon_{IAM_{s,c}} * \varepsilon_{LP_{s,c}}$ taken from Fig. 10. The estimated median optical efficiency of the LSC under direct radiation is 2.05% for TM, 2.23% for TS, 1.44% for BS, and 1.53% for BM.

4.3. Making predictions

Assuming we can achieve improved production of the light-guides with QY of 98%, we can use the grey-box simulation model to prepare a lookup-table of the yearly predicted performance of the SONOB demonstrator LSC plate for different climates, tilts and orientations. Table 3 shows the predicted yearly electric energy generation for Amsterdam, The Netherlands for the case of an LSC panel, a silicon-based semi-transparent PV panel and a bifacial PV device used in the SONOB program. The simulations were conducted with tilts and orientations in 10° increments.

Due to restricted space we only show the results for the East side of the of the sky hemisphere (from 0° to 180° azimuth), but because of the symmetry of the sky, these orientations can be used for predictions for the West side accordingly (the more complete data including the performance of the LSC panel with poor dye dispersion, may be found in the SI as Table S1). The results show that the LSC behaves similarly to the bifacial PV in terms of effect of tilt and orientation. Its relative performance is less sensitive to different orientations than a mono-facial PV system because it can utilize the

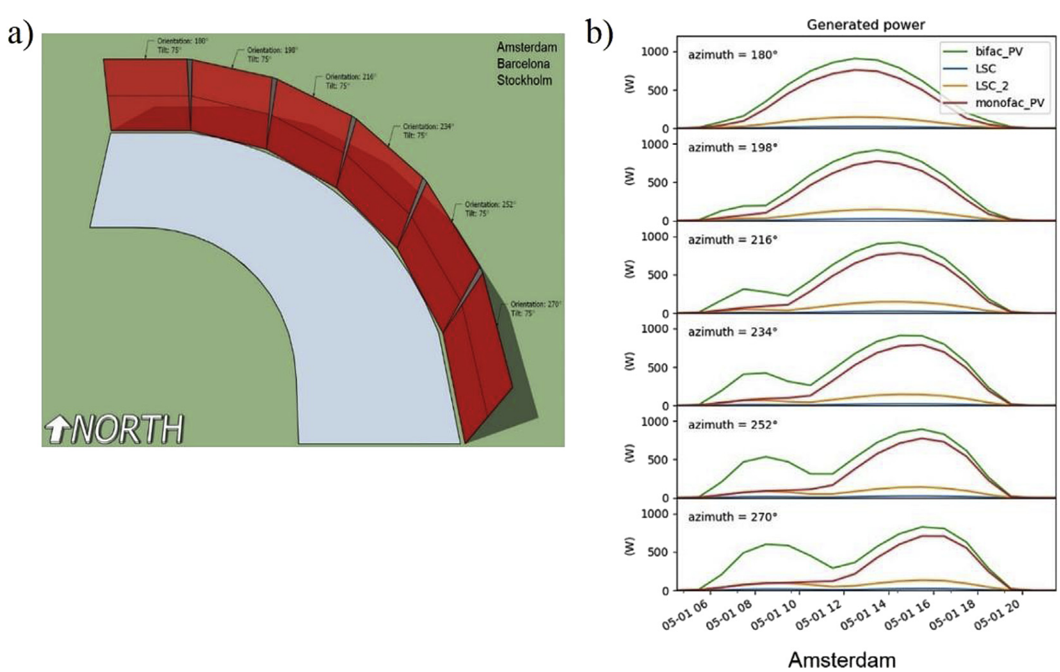

Fig. 11. a) Geometry of an LSC solar noise barrier near a corner of a road with different orientations ranging from Azimuth = 180° (south) to 270° (west). b) Simulated power output of the LSC solar noise barrier segments equipped with either bifacial, monofacial PV (bifac_PV and monofac_PV), or LSC with the faulty and the improved dye (LSC and LSC2).

Table 4
Estimated yearly electric energy generation in kWh/year for different tilts and orientations in a) Stockholm, b) Barcelona.

a) **Stockholm, LSC, QY=98%, ηPV=18%** Panel orientation (°)

Panel tilt (°)	~360	~350	~340	~330	~320	~310	~300	~290	~280	~270	~260	~250	~240	~230	~220	~210	~200	~190	~180
	0	10	20	30	40	50	60	70	80	90	100	110	120	130	140	150	160	170	180
0	158	158	158	158	158	158	158	158	158	158	158	158	158	158	158	158	158	158	158
10	144	144	145	146	147	149	151	153	155	157	160	162	164	167	168	170	171	172	172
20	131	131	132	134	136	140	143	147	151	156	160	165	169	173	176	178	181	182	182
30	120	121	122	125	129	133	138	144	149	155	161	166	172	176	181	184	187	188	189
40	113	114	117	120	125	131	137	143	149	155	161	167	173	178	182	186	189	191	192
50	113	115	118	123	129	134	140	146	151	157	162	167	173	178	183	187	190	193	194
60	124	125	128	133	137	142	147	151	155	159	163	168	173	178	183	187	190	192	193
70	139	140	142	145	148	151	154	156	158	161	164	168	172	176	180	183	185	187	188
80	154	155	156	158	159	160	161	161	162	163	165	167	169	172	174	176	178	179	179
90	168	169	169	169	169	168	167	165	164	164	163	164	165	166	167	167	168	168	168

b) **Barcelona, LSC, QY=98%, ηPV=18%** Panel orientation (°)

Panel tilt (°)	~360	~350	~340	~330	~320	~310	~300	~290	~280	~270	~260	~250	~240	~230	~220	~210	~200	~190	~180
	0	10	20	30	40	50	60	70	80	90	100	110	120	130	140	150	160	170	180
0	251	251	251	251	251	251	251	251	251	251	251	251	251	251	251	251	251	251	251
10	233	234	234	236	238	240	242	245	248	251	254	257	259	261	263	265	266	267	267
20	212	212	214	217	221	225	230	236	241	247	252	257	262	266	270	273	276	277	278
30	192	193	195	199	205	211	219	227	234	242	249	255	262	268	273	278	282	284	285
40	178	179	182	186	193	201	210	220	228	237	244	252	260	267	274	279	283	286	287
50	170	171	174	180	187	197	207	216	225	233	241	249	257	264	270	276	280	283	283
60	170	171	175	182	190	199	209	217	225	232	239	246	253	259	264	268	272	274	275
70	177	179	185	192	199	207	214	221	226	232	237	242	246	250	253	256	259	261	262
80	197	199	203	208	213	217	222	226	229	232	235	237	239	240	241	242	243	243	243
90	221	222	224	226	228	229	231	232	232	233	232	231	230	228	226	225	223	221	221

irradiance on both sides of the panel. This is beneficial for such applications as solar barriers near highways, where tilt and orientation of the panels is not optimized for electricity production, but is dictated by the primary use of the device. This behavior can be observed in more detail when looking at the power output on an hourly level for a clear day in Fig. 11 (and Fig. S4 for the other climates). Here, hourly simulated power outputs are shown on a sunny day for sound barrier panels in a corner of a road. Each barrier segment has a different orientation, but the same 15° tilt compared to vertical, which is typical for noise barriers. Similar performance predictions for panels located in the climates of Stockholm, Sweden and Barcelona, Spain were also made, also using IWEC (International Weather for Energy Calculation) weather files. The results are summarized in Table 4.

The overall absolute performance of the LSC panels are naturally inferior to the output of conventional PV, as one would expect. However, one can compensate for this difference in output with the dramatically enhanced aesthetics, robustness, transparency and reduced investment costs afforded by these panels.

5. Conclusions

Two simulation models are combined with experimental data to predict the performance of large scale luminescent solar concentrators at various European locations. Calculations using a ray-tracing design revealed that the performance of the large scale SONOB noise barrier installed in Den Bosch, the Netherlands, was hampered by sub-optimal distribution of the organic fluorescent dyes in the PMMA-based lightguide and mounting frame design. Simulations suggest that if the lightguides could be produced with better dye solubilization and more amenable frame geometry, a 6–9 fold increase in power output can be achieved, making the LSC a viable option for deployment in the built environment as a colorful solar energy generator.

Calculations using the grey-box model demonstrated the impact of angle of light incidence on performance and, given appropriate lighting conditions as input parameters, detailed predictions can be made for performance of large-scale LSC devices. The results of the case studies in three cities suggest absolute outputs of the LSC device are considerably lower than traditional silicon based semi-transparent PV panels or bifacial PV panels, as would be expected. However, such large-scale LSCs could still be viable for use in urban settings, serving a function such as a visually attractive noise barrier or other construction element that also produces electricity for local use, performing similarly in direct and diffuse light, maintaining transparency and enabling dual-side light absorption and light guiding performance even when spray painted, a robust structure, all this with a potentially short payback time on the additional components. This paper lays the groundwork for the further exploitation of the LSC device, and completes the series based on the experimental noise barrier prototypes.

Author contribution

All authors contributed to the writing of this paper.

Declaration of competing interest

The authors declare that they have no known competing financial interests or personal relationships that could have appeared to influence the work reported in this paper.

Acknowledgments

The SONOB project has been supported by the Dutch Government through the TKI ZEGO program. The authors would also like to acknowledge the other project partners: van Campen Industries BV, Heijmans Wegen BV, and Airbus Defense and Space for their support and the city of Den Bosch for making the test location available.

Appendix A. Supplementary data

Supplementary data to this article can be found online at https://doi.org/10.1016/j.renene.2019.11.102.

References

[1] J.A. Levitt, W.H. Weber, Materials for luminescent greenhouse solar collectors, Appl. Opt. 16 (10) (1977) 2684–2689.
[2] J.S. Batchelder, A.H. Zewail, T. Cole, Luminescent solar concentrators. 1: theory of operation and techniques for performance evaluation, Appl. Opt. 18 (18) (1979) 3090–3110.
[3] W.G.J.H.M. van Sark, K.W.J. Barnham, L.H. Slooff, A.J. Chatten, A. Büchtemann, A. Meyer, S.J. McCormack, R. Koole, D.J. Farrell, R. Bose, et al., Luminescent solar concentrators - a review of recent results, Opt. Express 16 (26) (2008) 21773.
[4] B. McKenna, R.C. Evans, Towards efficient spectral converters through materials design for luminescent solar devices, Adv. Mater. 29 (28) (2017) 1606491.
[5] M.G. Debije, P.P.C. Verbunt, Thirty years of luminescent solar concentrator Research: solar energy for the built environment, Adv. Energy Mater. 2 (1) (2012) 12–35.
[6] M.G. Debije, V.A. Rajkumar, Direct versus indirect illumination of a prototype luminescent solar concentrator, Sol. Energy 122 (2015) 334–340.
[7] A. Reinders, M.G. Debije, A. Rosemann, Measured efficiency of a luminescent solar concentrator PV module called leaf roof, IEEE J. Photovolt. 7 (2017) 1663–1666.
[8] B. Vishwanathan, A.H.M.E. Reinders, D.K.G. de Boer, L. Desmet, A.J.M. Ras, F.H. Zahn, M.G. Debije, A comparison of performance of flat and bent photovoltaic luminescent solar concentrators, Sol. Energy 112 (2015) 120–127.
[9] A. Reinders, R. Kishore, L. Slooff, W. Eggink, Luminescent solar concentrator photovoltaic designs, Jpn. J. Appl. Phys. 57 (8) (2018) 1–10.
[10] V.A. Rajkumar, C. Weijers, M.G. Debije, Distribution of absorbed heat in luminescent solar concentrator lightguides and effect on temperatures of mounted photovoltaic cells, Renew. Energy 80 (2015) 308–315.
[11] M.G. Debije, Solar energy collectors with tunable transmission, Adv. Funct. Mater. 20 (9) (2010) 1498–1502.
[12] R.R. Lunt, V. Bulovic, Transparent, near-infrared organic photovoltaic solar cells for window and energy-scavenging applications, Appl. Phys. Lett. 98 (2011) 113305.

[13] C. Yang, R.R. Lunt, Limits of visibly transparent luminescent solar concentrators, Adv. Opt. Mater. 5 (8) (2017) 1–10.
[14] F.M. Vossen, M.P.J. Aarts, M.G. Debije, Visual performance of red luminescent solar concentrating windows in an office environment, Energy Build. 113 (2016) 123–132.
[15] J.A.H.P. Sol, G.H. Timmermans, A.J. van Breugel, A.P.H.J. Schenning, M.G. Debije, Multistate luminescent solar concentrator "smart" windows, Adv. Energy Mater. 8 (2018) 1702922.
[16] W. van Sark, P. Moraitis, C. Aalberts, M. Drent, T. Grasso, Y. L'Ortije, M. Visschers, M. Westra, R. Plas, W. Planje, The "electric Mondrian" as a luminescent solar concentrator demonstrator case study, Sol. RRL 1 (3–4) (2017) 1600015.
[17] J.A.H.P. Sol, V. Dehm, R. Hecht, F. Würthner, A.P.H.J. Schenning, M.G. Debije, Temperature-responsive luminescent solar concentrators: tuning energy transfer in a liquid crystalline matrix, Angew. Chem. Int. Ed. 57 (4) (2018) 1030–1033.
[18] C. Corrado, S.W. Leow, M. Osborn, I. Carbone, K. Hellier, M. Short, G. Alers, S.A. Carter, Power generation study of luminescent solar concentrator greenhouse, J. Renew. Sustain. Energy 8 (4) (2016) 1–11.
[19] L.H. Slooff, E.E. Bende, A.R. Burgers, T. Budel, M. Pravettoni, R.P. Kenny, E.D. Dunlop, A. Büchtemann, A luminescent solar concentrator with 7.1% power conversion efficiency, Phys. Status Solidi R 2 (6) (2008) 257–259.
[20] J.C. Goldschmidt, M. Peters, A. Bösch, H. Helmers, F. Dimroth, S.W. Glunz, G.P. Willeke, Increasing the efficiency of fluorescent concentrator systems, Sol. Energy Mater. Sol. Cells 93 (2) (2009) 176–182.
[21] L. Desmet, A.J.M. Ras, D.K.G. De Boer, M.G. Debije, Monocrystalline silicon photovoltaic luminescent solar concentrator with 4.2% power conversion efficiency, Opt. Lett. 37 (2012) 3087–3089.
[22] M. Kanellis, M.M. de Jong, L. Slooff, M.G. Debije, The solar noise barrier project: 1. Effect of incident light orientation on the performance of a large-scale luminescent solar concentrator noise barrier, Renew. Energy 103 (2016) 647–652.
[23] M.G.M.G. Debije, C. Tzikas, V.A.V.A. Rajkumar, M.M. de Jong, M. de Jong, The solar noise barrier project: 2. The effect of street art on the performance of a large scale luminescent solar concentrator prototype, Renew. Energy 113 (2017) 1288–1292.
[24] M.G. Debije, C. Tzikas, M.M. de Jong, M. Kanellis, L.H. Slooff, The solar noise barrier project: 3. The effects of seasonal spectral variation, cloud cover and heat distribution in full-scale luminescent solar concentrator panels, Renew. Energy 116 (2017) 335–343.
[25] M. Carrascosa, S. Unamuno, F. Agullo-Lopez, Monte Carlo simulation of the performance of PMMA solar collectors, Appl. Opt. 22 (20) (1983) 3236–3241.
[26] A.J. Chatten, K.W.J. Barnham, B.F. Buxton, N.J. Ekins-Daukes, M.A. Malik, A new approach to modelling quantum concentrators, Sol. Energy Mater. Sol. Cells 75 (2003) 363–371.
[27] D. Sahin, B. Ilan, D.F. Kelley, Monte-carlo simulations of light propagation in luminescent solar concentrators based on semiconductor nanoparticles, J. Appl. Phys. 110 (2011) 33108.
[28] A. Kerrouche, D.A. Hardy, D. Ross, B.S. Richards, Luminescent solar concentrators: from experimental validation of 3D ray-tracing simulations to coloured stained-glass windows for BIPV, Sol. Energy Mater. Sol. Cells 122 (2014) 99–106.
[29] L.R. Wilson, B.S. Richards, Measurement method for photoluminescent quantum yields of fluorescent organic dyes in polymethyl methacrylate for luminescent solar concentrators, Appl. Opt. 48 (2) (2009) 212.
[30] G. Seybold, G. Wagenblast, New perylene and violanthrone dyestuffs for fluorescent collectors, Dyes Pigments 11 (1989) 303–317.
[31] P.P.C. Verbunt, T.M. de Jong, D.K.G. de Boer, D.J. Broer, M.G. Debije, Anisotropic light emission from aligned luminophores, Eur. Phys. J. Appl. Phys. Appl. Phys. 67 (01) (2014) 10201.
[32] P.P.C. Verbunt, C. Sánchez-Somolinos, D.J. Broer, M.G. Debije, Anisotropic light emissions in luminescent solar concentrators–isotropic systems, Opt. Express 21 (S3) (2013) A485.
[33] A.R. Burgers, L.H. Slooff, R. Kinderman, J.A.M. van Roosmalen, Modeling of luminescent solar concentrators by ray-tracing, in: 20th European Photovoltaic Solar Energy Conference, WIP Munich, Germany, 2005, pp. 394–397.
[34] M.G. Debije, P.P.C. Verbunt, B.C. Rowan, B.S. Richards, T. Hoeks, Measured surface loss from luminescent solar concentrator waveguides, Appl. Opt. 47 (36) (2008) 6763–6768.
[35] R.M. Ahmed, Optical study on poly(methyl methacrylate)/poly(vinyl acetate) blends, Int. J. Photoenergy 2009 (2009).
[36] M.J. Kastelijn, C.W.M. Bastiaansen, M.G. Debije, Influence of waveguide material on light emission in luminescent solar concentrators, Opt. Mater. 31 (11) (2009) 1720–1722.
[37] SunEarthTools.com. Last accesses April 24, 2019.
[38] PVEducation.org. Last accesses April 24, 2019.
[39] A. Jain, A. Kapoor, Exact Analytical Solutions of the Parameters of Real Solar Cells Using Lambert W -Function, vol. 81, 2004, pp. 269–277.
[40] L.H. Slooff, S. Verkuilen, M.M. De Jong, M. Kanellis, M.G. Debije, H.W.B. V, S.E. Buildings, Luminescent solar noise barrier – large scale testing and modeling, in: 2016 European PV Solar Energy Conference and Exhibition, EU PVSEC, Munich, Germany, 2016, pp. 1375–1378.
[41] E.E. Neuteboom, S.C.J. Meskers, E.W. Meijer, R.A.J. Janssen, Photoluminescence of self-organized perylene bisimide polymers, Macromol. Chem. Phys. 205 (2) (2004) 217–222.
[42] M.G. Debije, M.-P. Van, P.P.C. Verbunt, D.J. Broer, C.W.M. Bastiaansen, The effect of an organic selectively-reflecting mirror on the performance of a luminescent solar concentrator, in: 24th European Solar Energy Conference, vol. 93, 2009, pp. 373–376.
[43] T.S. Bohlin, Practical Grey-Box Process Identification: Theory and Applications, Springer Verlag, London, 2006.
[44] W. De Soto, S.A. Klein, W.A. Beckman, Improvement and validation of a model for photovoltaic array performance, Sol. Energy 80 (1) (2006) 78–88.
[45] G. Makrides, B. Zinsser, M. Norton, G.E. Georghiou, Performance of photovoltaics under actual operating conditions, in: V. Fthenakis (Ed.), Third Generation Photovoltaics, IntechOpen, 2010, p. 34.
[46] J.K. Kaldellis, M. Kapsali, K.A. Kavadias, Temperature and wind speed impact on the efficiency of PV installations. Experience obtained from outdoor measurements in Greece, Renew. Energy 66 (2014) 612–624.
[47] T. Dierauf, A. Growitz, S. Kurtz, C. Hansen, T. Dierauf, A. Growitz, S. Kurtz, C. Hansen, Weather-Corrected Performance Ratio, Technical Report NREL/TP-5200-57991, 2013.